atmosphere

MDPI

Article

Deconstructing Global Observed and Reanalysis Total Cloud Cover Fields Based on Pacific Climate Modes

Petru Vaideanu [1,2,*], Monica Ionita [1,3,4], Mirela Voiculescu [5] and Norel Rimbu [1]

[1] Alfred Wegener Institute Helmholtz Centre for Polar and Marine Research, 27570 Bremerhaven, Germany
[2] Faculty of Physics, University of Bucharest, 077125 Măgurele, Romania
[3] Emil Racovita Institute of Speleology, Romanian Academy, 400006 Cluj-Napoca, Romania
[4] Faculty of Forestry, Ștefan cel Mare University, 720229 Suceava, Romania
[5] Department of Chemistry, Physics and Environment, University "Dunărea de Jos", 800008 Galaţi, Romania
* Correspondence: petru.cosmin.vaideanu@awi.de; Tel.: +40-754-532-389

Abstract: Clouds are notoriously difficult to simulate. Here, we separate and quantify the impact of Pacific climate modes on total cloud cover (TCC) variability, using reliable satellite observations together with state-of-the art reanalysis outputs, over the 1979–2020 period. The two most prominent modes of annual TCC variability show intense loadings over the Pacific basin and explain most of the variance in what could be considered the "signal" in satellite TCC data. Canonical correlation analysis (CCA) provides coupled TCC—sea surface temperature (SST) patterns that are linked to the Eastern Pacific (EP) ElNiño—Southern Oscillation (ENSO) and the Central Pacific (CP) ENSO in a physically consistent manner. The two ENSO modes dominate global coupled SST–TCC variability with the footprint of the CP ENSO explaining roughly half of the variance induced by the EP ENSO among these coupled fields. Both the EP and the CP ENSO exert an influence on Pacific decadal TCC variability. The impact of both ENSO modes on global total cloud cover variability is amplified by two positive feedbacks. These results could be used as a reference for model investigations on future projections of coupled TCC—SST variability responses to the CP and the EP ENSO.

Keywords: total cloud cover; Eastern Pacific El-Niño; Central Pacific El-Niño; sea surface temperature; convection

Citation: Vaideanu, P.; Ionita, M.; Voiculescu, M.; Rimbu, N. Deconstructing Global Observed and Reanalysis Total Cloud Cover Fields Based on Pacific Climate Modes. *Atmosphere* **2023**, *14*, 456. https://doi.org/10.3390/atmos14030456

Academic Editor: Jimy Dudhia

Received: 20 January 2023
Revised: 12 February 2023
Accepted: 21 February 2023
Published: 24 February 2023

1. Introduction

Clouds have a complex influence on the Earth's radiation budget, as seen in [1], and predicting their behavior is problematic as doing so has generated the largest uncertainties in climate projections for decades [2–5]. Thus, analyzing large-scale satellite total cloud cover data is of great importance. However, the data are also not perfect, and issues affecting satellite cloud measurements are numerous, including biases from top-down viewing angles, artificial trends connected to instrument degradation and orbital decay [6], changes in the number of observing satellites [7], data intercalibration issues [8], cloud overlap [9] or biases connected to changes in viewing times and in the diurnal cloud cycle [10,11].

Sea surface temperature (SST) is key factor in large-scale cloud formation and evolution [12]. SST—cloud interactions manifest through a variety of physical processes and feedbacks which generate large discrepancies between climate models with regard to climate sensitivity [13–15]. The El-Niño—Southern Oscillation (ENSO) [16–18] is the most prominent mode of SST variability in the climate system and has a global socio-economic impact [19–21]. During the last decade, an increasing number of studies have focused on two types of ENSO: (1) conventional, canonical or Eastern Pacific (EP) ENSO, for which the maximum SST variability manifests in the eastern tropical Pacific [22] and (2) the Central Pacific (CP) El-Niño [23], also known as the El-Niño Modoki [24], Warm Pool El-Niño [25] or date line El-Niño [26], with the maximum SST variability being located over the Central

Pacific. In this paper, the generic term "CP ENSO" is used to refer to the latter. It has been proposed that the EP-type and the CP-type of ENSO have distinct impacts on regional temperature, precipitation and storm track activity [24]. It has been observed in recent decades that the CP ENSO occurs more, but that its duration is shorter than that of the EP ENSO [27]. This recent increase in the CP ENSO frequency, which is very likely higher than any other similar period over the last 400 years [28], was attributed to climate change [23]. As anthropogenic warmings will intensify, it is argued that these events will become more frequent, to the detriment of the EP ENSO [18,24].

The impact of the conventional ENSO on Pacific cloud variability has been the subject of many previous studies, e.g., [19,29–33]. Cloud projections in CMIP5 models were analyzed in relation to the EP ENSO [34] and decadal internal variability [35]. The CP ENSO was investigated in relation to changes in high cloud cover [36] and local changes in precipitation patterns [37,38]. However, the complexity of the ENSO phenomenon is still a current and intriguing topic in the climate community [18,20,23].

In this study, we link the EP ENSO and the CP ENSO to observed coupled TCC—SST variability on a global scale. We focus on addressing three questions: What are the differences between the EP and the CP ENSO in their relation to TCC? What is the quantitative relevance of each ENSO mode in relation to coupled TCC—SST variability? What is the quality of the satellite data when compared to outputs from reanalysis data, in relation to interannual and decadal TCC? Section 2 includes a description of the observational data and of the statistical methods used in this study. In Section 3, the main results of this study are presented. Discussions and conclusions are presented in Section 4.

2. Data and Methods

2.1. Data

Observed TCC data were obtained from two indented satellite measurements from the International Satellite Cloud Climatology Project (ISCCP) [39,40] and the Pathfinder Atmospheres–Extended (PATMOS-x) fields [41]. The ISCCP and PATMOS-x datasets were used in many studies on the causes and mechanisms of cloud changes [42–46]. However, as with many retrieval fields, these datasets are accompanied by uncertainties. These uncertainties are related to changes in the geostationary satellite zenith angle [7], changes in the equatorial crossing time [10] or changes in calibration [8]. Artefacts in the ISCCP and the PATMOS-x data have been extensively addressed and corrected by [11]. For this study, we used the corrected versions of the IPSCC and PATMOS-x TCC fields, distributed on a $2.5^{o} \times 2.5^{o}$ global grid, from 1984–2009. The corrected versions of the ISCCP and PATMOS-x total cloud cover data were obtained from the NCAR Research Data Archive available at https://rda.ucar.edu/datasets/ds741.5/ (accessed on 1 October 2019).

To compare the results obtained with the observed satellite measurements, we also make use of TCC data on the 1979–2020 period obtained by the latest state-of-the-art reanalysis product (ERA5R) from the European Centre for Medium-Range Weather Forecasts (ECMWF) [47]. The ERA5 Reanalysis project is the latest example of ECMWF reanalysis and provides a variety of atmospheric and climate variables. It uses a state-of-the-art modelling and data assimilation system based on a large variety of historical observations of pressure, temperature, humidity and other variables. Compared to ERA-Interim, ERA5R has many advantages in terms of parametrization and assimilation and could provide a more realistic representation of cloud physical processes [47]. ERA5R also provides sea level pressure (SLP) and 10 m wind global fields at a resolution of $1^{o} \times 1^{o}$. Gridded ERA5R data are available for download at https://apps.ecmwf.int/data-catalogues/era5/?class=ea (accessed on 1 October 2019).

SST data on the period 1870 to 2020were provided by the United Kingdom Met Office's (UKMO) through the Hadley Centre Sea Ice and Sea Surface Temperature dataset (HadISST) [48] on a grid with a $1^{o} \times 1^{o}$ resolution. The HadISST data are available at https://www.metoffice.gov.uk/hadobs/hadisst/ (accessed on 1 October 2019).

For the observed total precipitation rate (TPR) field, we used data on the 1979–2020 period obtained by the Combined Precipitation Data Set provided by the Global Precipitation Climatology Project (GPCP) [49], which is distributed at a resolution of 1.5° × 1.5°. The data are available at https://psl.noaa.gov/data/gridded/data.gpcp.html (accessed on 1 October 2019).

To measure the evolution of the EP ENSO, we used the Niño3 index. The Niño3 and the Niño4 time series are highly correlated (r > 0.8, >95% significance level). There is still no consensus on the proper index with which to describe CP ENSO evolution [50–52]. In this study, we used the Trans-Niño Index (TNI), which is defined as the difference of the normalized SST anomalies from the Niño 4 and the Niño 1+ Niño 2 regions [53]. The low correlation between the TNI and the Niño3 Index (r < 0.15, <90% significance level) supports the idea that these two time series are describe the distinct evolutions of these two types of ENSO-like events. The Niño3 Index and the TNI Index were obtained from http://www.esrl.noaa.gov/psd/data/climateindices/list/ (accessed on 1 October 2019).

2.2. Initial Pre-Filter of the Data

In a preliminary stage, for all datasets used, monthly anomalies from the annual cycle were calculated relative to the 1984–2009 period, and then annual means were computed. Cloud trends in satellite data may be the result of various measurement artefacts [54,55]. In order to isolate the possible footprints of internal modes of variability, the trends in satellite and reanalysis TCC data were removed by applying linear detrending. Because the variability of the global SST field is dominated by the spatially quasi-uniform warming trend, the SST trend is removed by subtracting the annual global average from each grid point. The removal of the trend facilitated the identification of the coupled TTC–SST footprints of Pacific internal variability on these fields. However, similar results were obtained when the trend in the SST data was not removed (Figure S2).

2.3. Multivariate Statistical Methods

The dominant modes of TCC were derived by using the Empirical Orthogonal Functions (EOF) method [56].This technique applies orthogonal transformation to transform a set of observations of correlated variables into a set of values of non-correlated linear variables. The uncorrelated variables represent linear combinations of the initial ones. The first main component explains the maximum amount of variance among the original variables; the second one explains the maximum amount of remaining variance, which is not explained by the first component, and so on. As it is essentially based on pattern separation, EOF analysis is an efficient method to investigate the spatial and temporal variability of time series as it extends over relatively large areas. All the analyzed EOFs were past rule M for separation ("significance") [57] because the spacing between the eigenvalues were significantly larger than the sampling error for all analyzed EOFs (Table S1).

To identify coupled TCC–SST patterns, we employed Canonical correlation analysis (CCA) (von Storch and Zwiers, 1999). CCA is a powerful multivariate technique used to identify pairs of patterns with a maximum correlation between their associated time series. In other words, CCA determines the extent to which two phenomena, each described by a variable or a set of variables, are linked. Mathematically, CCA transforms pairs of originally centered vectors, X_0 and Y_0, into sets of new variables called canonical variables. The canonical correlations are determined by solving the eigenvalue equations:

$$\begin{cases} [C_{xx}]^{-1}[C_{xy}][C_{yy}]^{-1}[C_{yx}]\ W_x = \rho^2 W_x \\ [C_{yy}]^{-1}[C_{yx}][C_{xx}]^{-1}[C_{xy}]\ W_y = \rho^2 W_y \end{cases}$$

where C_{xx} and C_{yy} are the matrices of covariance for x and y, respectively,
$C_{xy} = C^{-1}{}_{yx}$ is the between-sets covariance matrix,
ρ^2 eigenvalues are the squared canonical correlations, and the eigenvectors,
W_x and W_y, are the normalized canonical correlation basis vectors.

As the core constraint of the method is the maximization of the correlation between time components, the corresponding patterns are provided by the method even if they do not explain large amount of variance in their fields, which means that the patterns explaining the largest percentage of variance do not necessarily appear in the first pairs. In order to increase this ratio and therefore to maximizes the effectiveness of CCA, each of the two initial fields (SST and TCC) was decomposed in a linear combination of EOFs and then was reconstructed based only on the first eight modes.

CCA is based on the distinction between the time evolution of patterns (the time series of consecutive pairs are uncorrelated). Therefore, CCA can be used to determine the footprint of a forcing factor on a given field, while distinct forcing factors are characterized by different temporal evolutions. The distinction between the TCC spatial structures associated with the EP ENSO and the CP ENSO in pairs derived through CCA was emphasized based on their specific SST footprint and also on their specific temporal evolution. The final assessment of the significance of the identified coupled patterns relied on their physical consistency.

The statistical significance of correlations and regressions were examined in relation to the (two-tailed) probability (p) value to obtain a similar correlation value by chance. In order to determine the exact degrees of freedom, the effective number of degrees of freedom used to calculate was computed with the following: $N_{ef} = N\ (1 - R_1R_2)/(1 + R_1R_2)$, in which N is the number of values of the time series and R_1 and R_2 represent the lag-one autocorrelation of each record [58].

3. Results

3.1. Dominant Modes of Global Total Cloud Cover Variability

The first two modes of TCC variability, derived through the EOF analysis of the annual TCC anomalies from ISCCP and PATMOS-x datasets extending over the 1984–2009 period and the ERA5 reanalysis data extending over the 1979–2020 period, are shown in Figure 1. The first main component explains the maximum amount of variance among the original variables; the second one explains the maximum amount of remaining variance, which is not explained by the first component, and so on.

The spatial structures of EOF1, identified by ISCCP (Figure 1a), PATMOS-x (Figure 1c) and ERA5 (Figure 1e), are qualitatively and quantitatively similar across most of the globe. They have the highest loadings in the tropical Pacific and can be characterized by a band of positive TCC anomalies extending from the west coast of Peru toward the Central Pacific, and by negative loadings in the Central, North East and South East Pacific. They also include positive anomalies over most of North America, Central Asia and the North north Atlantic that are more prominent in the ERA5 pattern (Figure 1e) and less intense in the PATMOS-x data (Figure 1c), but also negative values over the tropical Atlantic, extending to the north-eastern part of South America. Differences between the observed and reanalyzed EOF1 patterns are seen over parts of Australia, the north-western part of South America and the South Atlantic. The three associated time series (PC1, Figure 1g) are dominated by interannual variability and are highly correlated (r = 0.89, significant at the 99% level).

The spatial patterns of the second EOF, derived from ISCCP (Figure 1b) and PATMOS-x (Figure 1d) TCC data, and from ERA5 (Figure 1f), are similar across most of the globe, and are characterized by an equatorial dipole of TCC anomalies in the equatorial Pacific, with intense positive loadings in the central part and negative anomalies in the eastern sector. They also include an increase in cloudiness in the north-eastern part of South America extending to the tropical Atlantic, and a decrease in cloudiness over most of the North Atlantic. The associated PCs (Figure 1h) show no increasing trend, and their correlation coefficient is 0.77 (significant at the 99% level).

The maximum TCC positive anomalies of the spatial structures of both EOFs are located in the tropical Pacific, and their PCs are dominated by interannual variability. The combined variance explained by the first two modes, in the observational results, is 35% for ISCCP (Figure 1a,b) and 32% for the PATMOS-x fields (Figure 1c,d). A large part of the

distribution of the rest of the observed EOF variance (about 55%) is quasi-equally shared by a large number of modes, each explaining less than 5% of variance (Table S1), which suggests that these are associated with noise.

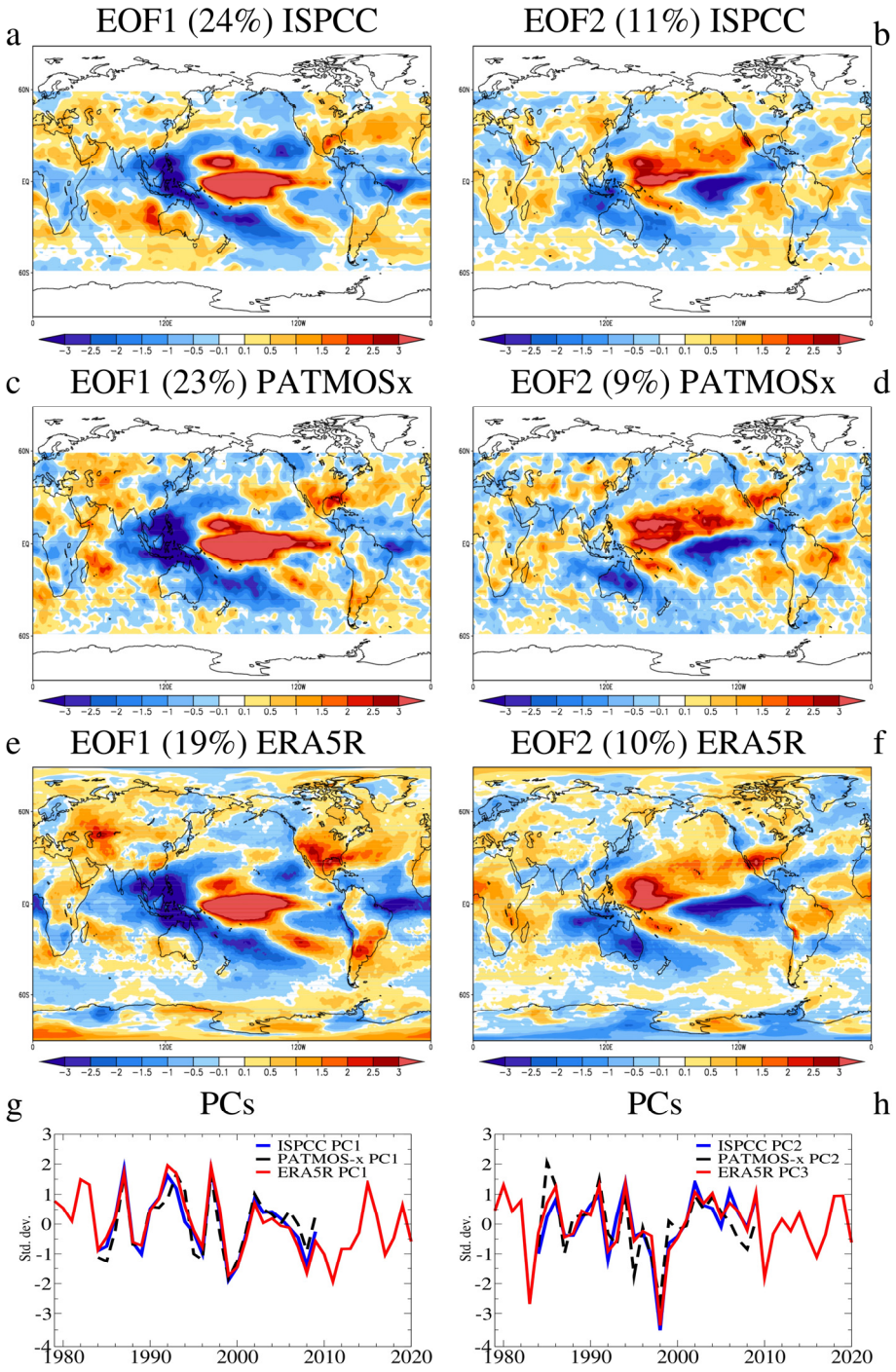

Figure 1. Global modes of TCC variability in detrended satellite and ERA5 reanalysis data. Left column: The spatial structure of the dominant mode (EOF1) of TCC variability (%) based on ISCCP (**a**), PATMOS-x (**c**) and ERA5 reanalysis (**e**) data with their associated time series (**g**). Right column: The second empirical orthogonal function (EOF2) of TCC variability (%) based on ISCCP (**b**) and PATMOS-x (**d**) data and the third EOF from ERA5 reanalysis (**f**) data, with their associated time series (**h**).

3.2. Observed Coupled SST-TCC Patterns Associated to Interannual Pacific Climate Variability

In order to identify globally observed SST–TCC pairs, two rounds of CCA were performed for the period 1984–2009 using the observed SST, one using corrected TCC anomalies from ISPCC data and the other using TCC data from PATMOS-x. The results shown in Figure 2 (for ISCCP) and Figure 3 (for PATMOS-x) and are summarized in Table 1. The percentage of variance explained by each spatial pattern provided by CCA is obtained as the average of the squared correlation coefficient (r2) between the time series provided by CCA and the reconstructed SST/TCC fields [58,59].

Table 1. The variances explained by the EP ENSO and the CP ENSO SST/TCC patterns from ISPCC (Figure 2) and PATMOS-x (Figure 3) satellite observations and ERA5 reanalysis (Figure 4).

CCA	Explained Variance (r^2) SST	Explained Variance (r^2) TCC	Correlation Coefficient PCs	Footprint	Correlation with the Associated Index	Projection on EOF1 1 = Identical Projection	Projection on EOF2/3 1 = Identical Projection	Projection on Decadal Variability Max Value = 1
ISPCC 3rd pair	20%	22%	0.98	EP ENSO	0.84	0.94	0.03	0.35
ISPCC 4th pair	7%	7%	0.97	CP ENSO	0.67	0.04	0.89	0.26
PATMOS-x 3rd pair	16%	17%	0.99	EP ENSO	0.8	0.79	0.02	0.29
PATMOS-x 4th pair	9%	8%	0.98	CP ENSO	0.73	0.01	0.71	0.21
ERA5 3rd pair	16%	13%	0.98	EP ENSO	0.91	0.95	0.02	0.25
ERA5 5th pair	7%	7%	0.97	CP ENSO	0.72	0.06	0.81	0.17

The spatial structures of the first two pairs identified through conducting two rounds of CCA explain less than 6% of the variance (Table S2), and are not of interest in our study due to their spatio-temporal characteristics.

The third and fourth coupled SST–TCC pairs, derived through CCA using the ISPCC TCC fields, are shown in Figure 2. The SST spatial structure of the third pair (Figure 2a) explains 20% of the total variance and is dominated by a band of positive anomalies located in the eastern tropical Pacific, which is surrounded by negative values, comprising the typical structure of the EP ENSO [16–18]. Its coupled TCC pattern (Figure 2e) is characterized by positive anomalies in the eastern-central Pacific and over the North and the South Atlantic, and by negative anomalies in the western-central Pacific, the north-east (NE) and the south-east (SE) Pacific. The TCC spatial structure explains 22% of the total cloud cover variance and projects strongly on EOF1 (Figure 1a) (projection coefficient of 0,94, where r = 1 is the maximum value and represents identical projection) (see Table 1). The corresponding time series (Figure 2c) are dominated by inter-annual variability and are significantly correlated with the Niño3 Index (r = 0.84). The maximum amplitude was in 1997–1998, when a strong EP ENSO event was recorded [60].The SST structure of the fourth pair (Figure 2b) explains 7% of the total variance and can be described by the following features: (i) the highest positive values, which are located in the Central Tropical Pacific; (ii) a horizontal V-shaped anomaly structure with positive values starting from the central tropical Pacific and extending toward the subtropics in both hemispheres; (iii) negative SST anomalies near the northwest coast of South America. These characteristics were identified as the SST signature of the CP ENSO in previous observational and numerical studies [23,24,50,61]. The associated TCC spatial structure (Figure 2f) has the highest loadings in the Central Pacific, with positive values in the Central Tropical Pacific and negative TCC anomalies in the eastern tropical Pacific, surrounded by positive TCC values in the subtropics. This feature is significantly distinct from any characteristic associated with the EP ENSO (Figure 2e). The TCC spatial structure explains 7% of the total variance

and projects strongly on EOF2 (Figure 1b). The association of the TCC structure with the CP ENSO is also supported by the associated PC-s of this pair (Figure 2d), which are significantly correlated (r = 0.67, significance level >95%) with the TNI, which is a very good measure for CP ENSO events [62].

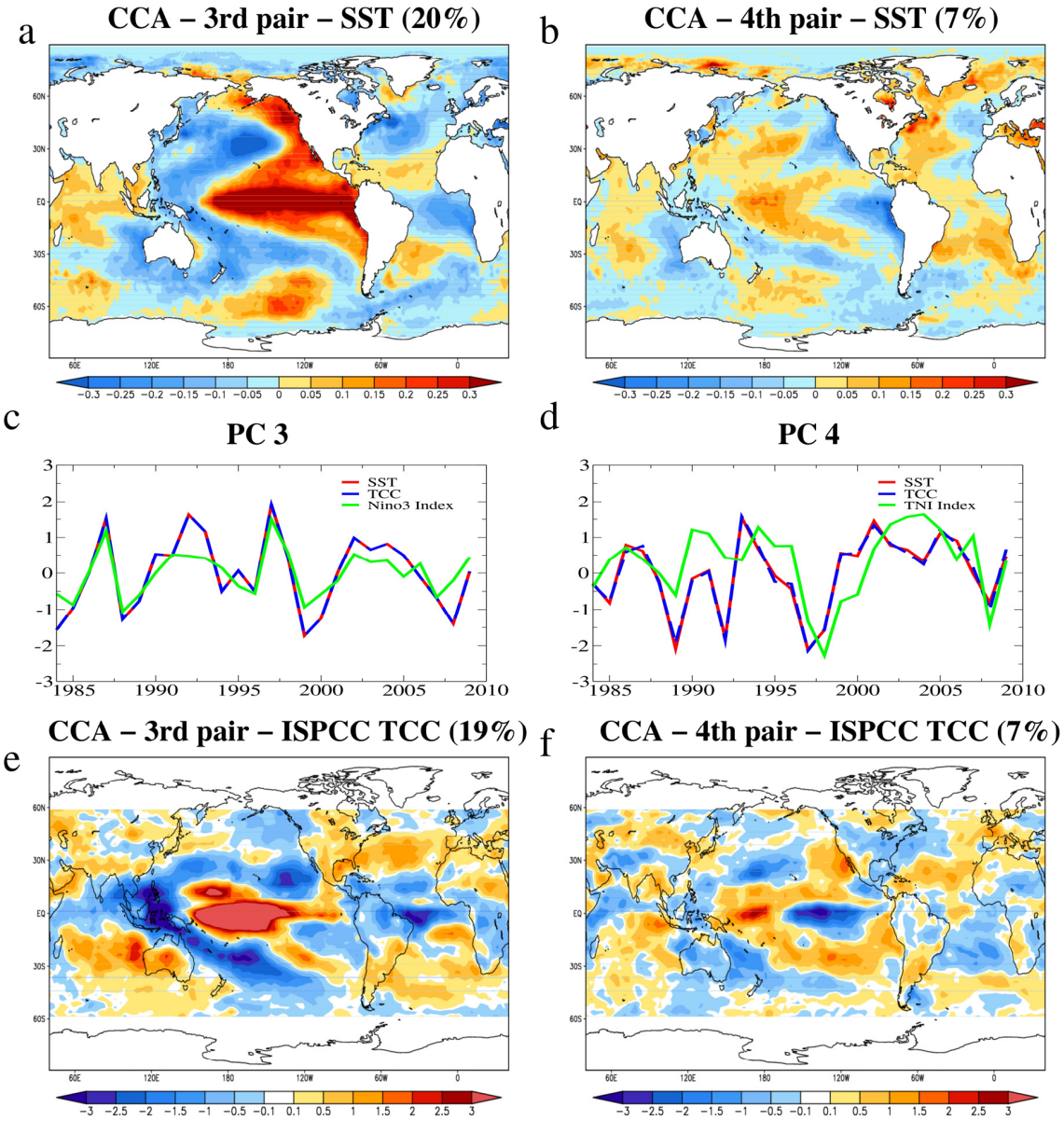

Figure 2. The EP ENSO and the CP ENSO footprints on global SST–TCC coupled fields, identified through CCA using ISPCC TCC data on the 1984–2009 period. The left column shows the third coupled SST (°C)—TCC (%) pair, the SST pattern (**a**), explaining 20% of variance, the TCC structure (**e**), explaining 19% of variance and the time series (**c**) associated with TCC (blue line) and SST (red line). The correlation with the Niño3 index (green line) is 0.81. The right column shows the fourth coupled SST (°C)—TCC (%) pair, the TCC pattern (**b**), explaining 7% of variance, the SST structure (**f**), explaining 7% of variance, and the time series(**d**) associated with TCC (blue line), and SST (red line). The correlation with the TNI Index (green line) is 0.61.

A similar CCA was performed using the PATMOS-x total cloud cover data (Figure 3). The associated temperature (cloud) pattern of the third SST–TCC (PATMOS-x) pair explains 16% (17%) of the total variance, whereas the temperature (cloud) spatial structure of the fourth pair explains 9% (8%) of the total variance (Table 1). The SST pattern of the third

pair (Figure 3a) is characteristic of the EP ENSO, with intense positive SSTs in the Eastern Tropical Pacific. The corresponding time series (Figure 3c) closely follow the Niño3 index (r = 0.8, significance level >95%). The associated TCC structure (Figure 3e) includes positive anomalies in the Eastern Tropical Pacific, in the North Atlantic and over most of North America, and includes intense negative anomalies in the central-western Pacific, similar to the EP ENSO footprint obtained using the ISPCC data (Figure 2e). Differences between the two observed TCC spatial structures associated with the EP ENSO are observed over Australia, parts of South America and Africa.

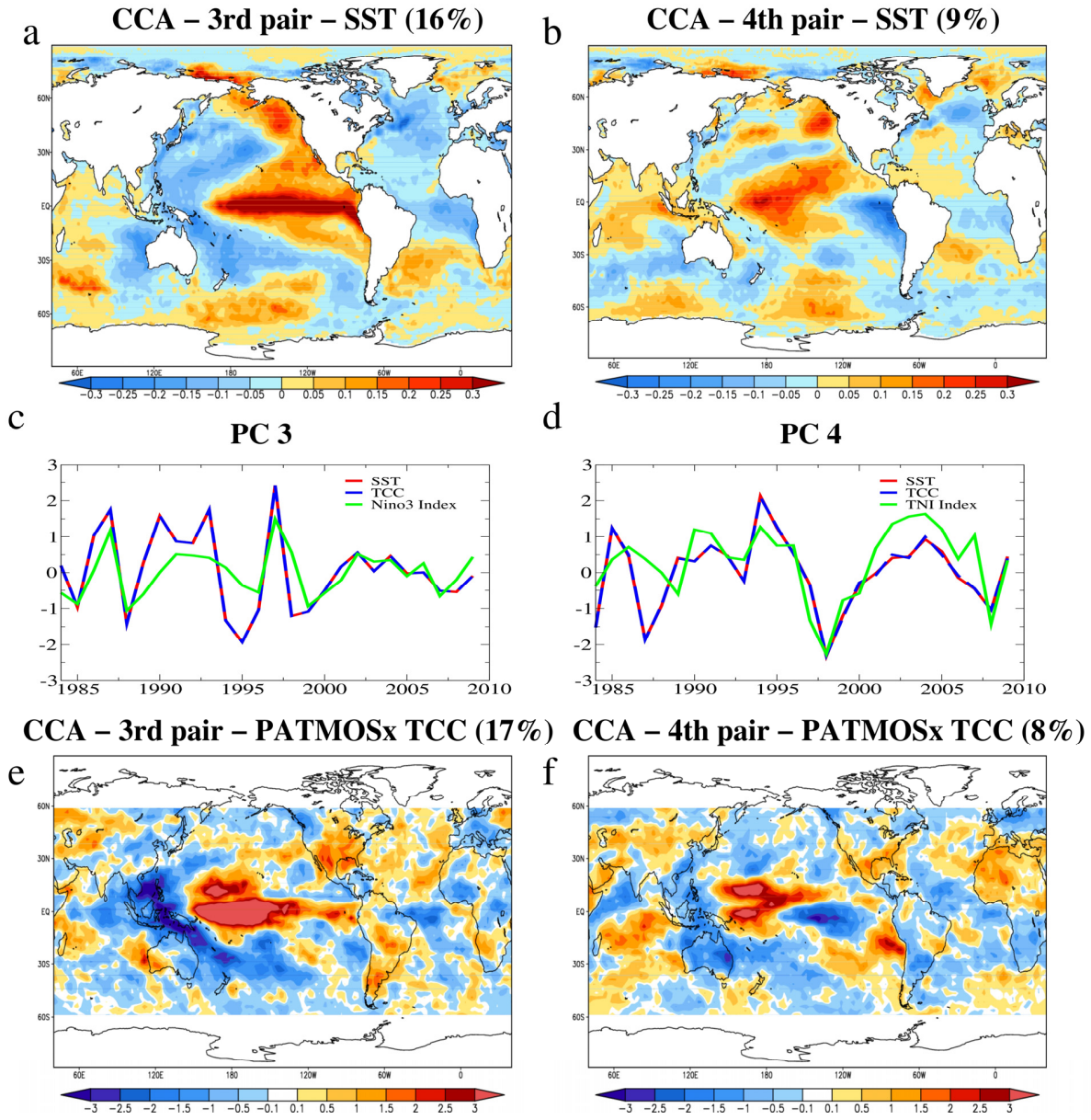

Figure 3. The EP ENSO and the CP ENSO footprints on global SST–TCC coupled fields, identified through CCA using PATMOS-x TCC data on the 1984–2009 period. The left column shows the third most coupled SST (°C)—TCC (%) pair, the SST pattern (**a**), explaining 16% of variance, the TCC structure (**e**), explaining 17% of variance and the time series (**c**) associated with TCC (blue line) and SST (red line). The correlation with the Niño3 index (green line) is 0.79. The *right column* shows the fourth most coupled SST (°C)—TCC (%) pair, the TCC pattern (**b**), explaining 9% of variance, the SST structure (**f**), explaining 8% of variance and the time series (**d**) associated with TCC (blue line) and SST (red line). The correlation with the TNI (green line) is 0.73.

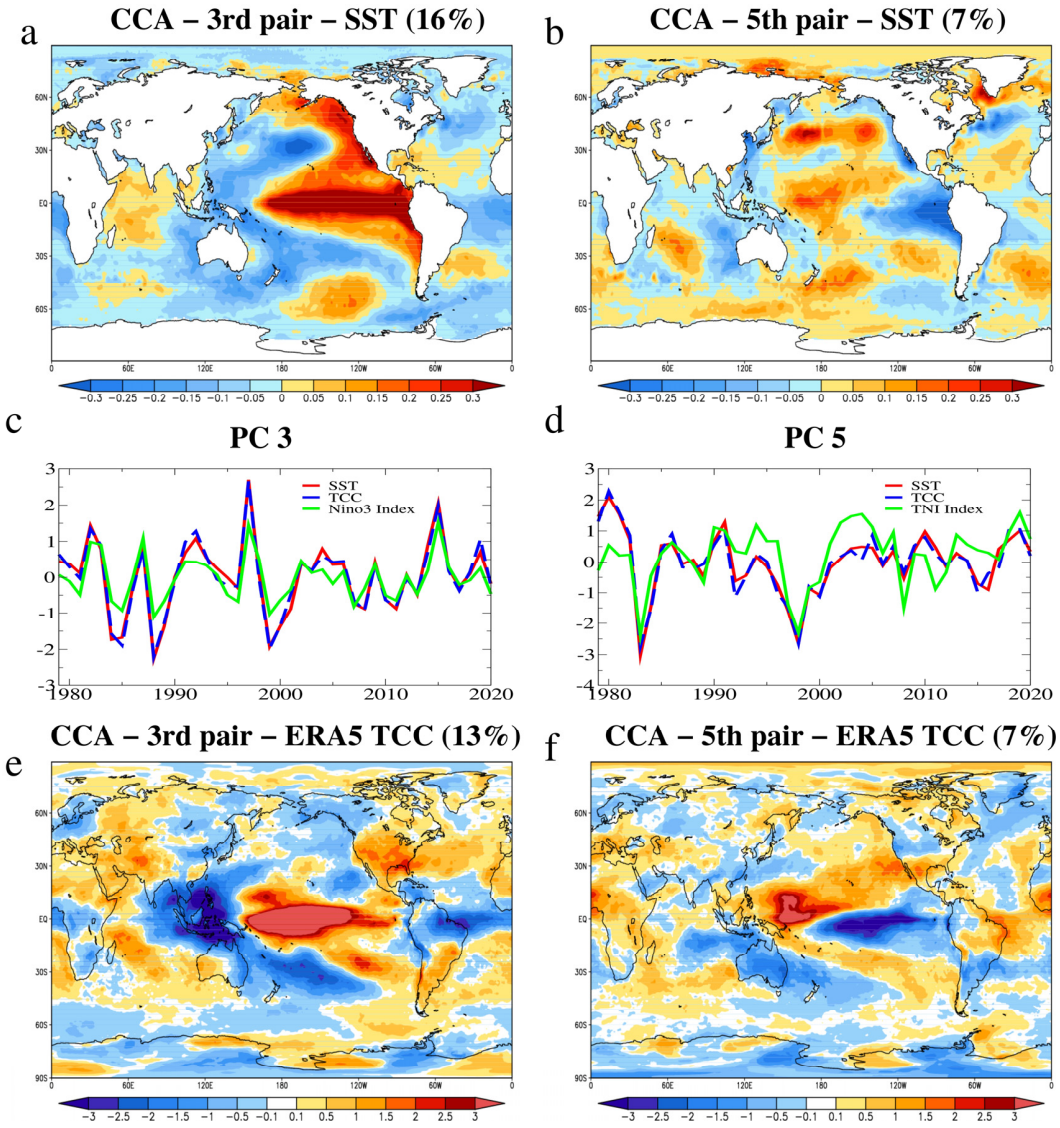

Figure 4. The EP ENSO (left) and the CP ENSO (right) footprints on global SST–TCC fields identified through CCA using ERA5 total cloud cover data on the 1979—2020 period. The left column shows the third most coupled TCC SST (°C)—TCC (%) pair identified through CCA using ERA5 TCC data, the TCC pattern (**a**), explaining 16% of variance, the SST structure (**c**), explaining 13% of variance and the time series (**e**) associated with TCC (blue line) and SST (red line). The correlation with the Niño3 index (green line) is 0.89. The right column shows the fifth most coupled SST (°C)—TCC (%) pair, the TCC pattern (**b**), explaining 7% of variance, the SST structure (**f**), explaining 7% of variance and the time series (**d**) associated with TCC (blue line) and SST (red line). The correlation with the TNI Index (green line) is 0.71.

The SST and the TCC spatial structures of the fourth pair (Figure 3b,f) can be characterized by an east–west dipole of SST/TCC anomalies located in the Tropical Pacific, with positive values in the Central Pacific and negative loadings in the east Pacific that more prominent than those in the CP ENSO pair obtained using the ISPCC data (Figure 2b,f). Their associated time series (Figure 3d) have a correlation coefficient of 0.73 (significant over 95% confidence level) with the TNI x, further supporting the association of this pair with the CP ENSO.

Both the ISCCP and the PATMO-x datasets capture the main features of the EP ENSO and the CP ENSO modes over the oceans, but the results obtained using the PATMOS-x data are more consistent with previous regional studies in North America [19], South

America [63] and Australia [64], indicating that this dataset is more suitable for regional investigations in terms of the ENSO (Figure S1). Together, the two global TCC spatial patterns explain more than 25% of the global cloud cover variance. TCC patterns associated with the CP ENSO (Figures 2e and 3e) project strongly on EOF1, while the TCC spatial structures associated with the CP ENSO (Figures 2f and 3f) project strongly on EOF2 (Table 1), indicating that the two ENSO modes have a profound impact on global total cloud cover variability.

3.3. Coupled SST- Reanalysis TCC Patterns Associated to Interannual Pacific Climate Variability

In order to test the robustness of the results within a different time frame, we also performed a CCA using the ERA5 reanalysis total cloud cover data on the 1979–2020 period, and the results are shown in Figure 4.

The SST spatial structure of the 3rd pair (Figure 4a) explains 16% of variance and resembles the EP ENSO, with a band of intense positive SSTs in the Eastern Tropical Pacific flanked by negative loadings and positively correlated with the associated TCC structures. The reanalyzed TCC spatial structure associated with the EP ENSO (Figure 4e) includes positive loadings in the Eastern Tropical Pacific, over most of North America and the North Atlantic, while negative anomalies are present over the Western Pacific, over the NE and the SE Pacific and over the tropical Atlantic. The reanalyzed EP ENSO TCC footprint is similar, quantitatively and qualitatively, over most of the globe, with both the ISPCC (Figure 2e) and PATMOS-x (Figure 3e) footprints, but resembles the one obtained using ISPCC data over land more. The associated time series (Figure. 4e) are significantly correlated with the Niño3 index (r = 0.91, >95% significance level). The SST structure of the 5th coupled pair (Figure 4d) is dominated by a dipole of anomalies in the Atlantic basin and intense positive loadings in the Central Pacific, which is typical for the CP ENSO. The coupled TCC pattern includes negative anomalies in the Eastern Tropical Pacific and positive anomalies in the Central Pacific, which is in very good agreement with the TCC pattern associated with the CP ENSO using the ISPCC (Figure 2f) and PATMOS-x (Figure 3f) data. The time series associated with the coupled patterns (Figure 4f) are significantly correlated with the TNI index (r = 0.72, >95% significance level).

Both TCC structures presented in Figure 4 are similar to the corresponding TCC structures identified in the ISPCC (Figure 2) and in the PATMOS-x (Figure 3) data and associated with the EP ENSO and the CP ENSO. This indicates that ERA5 reanalysis reproduces the formation and evolution of total cloud cover on a global scale fairly well. The close similarity between the TCC structures derived from satellite observations and from the reanalysis indicate that the observed results are relevant for global TCC variability across various time scales.

3.4. Coupled SST-TCC Patterns Associated to Decadal Pacific Variability

In order to facilitate the identification of the impact of decadal SST variability on the evolution of global cloud cover, three CCAs were performed between SST and TCC values from ISPCC, PATMOS-x and ERA5 reanalysis data, filtered by a 5-year running mean. The resulting pairs of interest are shown in Figure 5.

All three SST structures (Figure 5a–c) can be characterized by a horseshoe-like structure in the North Pacific with negative anomalies in the north-west surrounded by positive loadings, and an El-Niño like structure in the tropical Pacific. These features have been attributed previously to the positive phase of the Pacific Decadal Oscillation [65,66] or the North Pacific Gyre Oscillation [67]. The TCC pattern from the first pair obtained using ISCCP data (Figure 5a) is dominated by positive anomalies located in the Central Tropical Pacific, and by negative anomalies extending westward, which are positively correlated with the SSTs anomalies. Negative anomalies which are anti-correlated with the SSTs anomalies are observed in the north-east and south-east Pacific. These features have been previously associated with Pacific decadal SST variability [31]. The same characteristics can be observed in the TCC spatial structure obtained using PATMOS-x (Figure 5h) and

ERA5 (Figure 5i) data, but the negative anomalies are less prominent in the eastern and southern Pacific. The ISCCP—TCC pattern (Figure 5a) includes positive anomalies over the southern part of North America and the south eastern part of South America, while negative loadings are observed over most of northern South America and the north of Australia. These features were previously associated with positive decadal SST variations in the North Pacific [63] and were not captured so well in the pair obtained using the PATMOS-x and ERA5 data. Both the EP ENSO and the CP ENSO impact the evolution of decadal TCC variability in the Pacific basin (Table 1), with the EP ENSO being more prominent. This is in good agreement with previous studies that show that both the eastern and central expressions of ENSO play significant roles in modulating Pacific decadal variability [68].

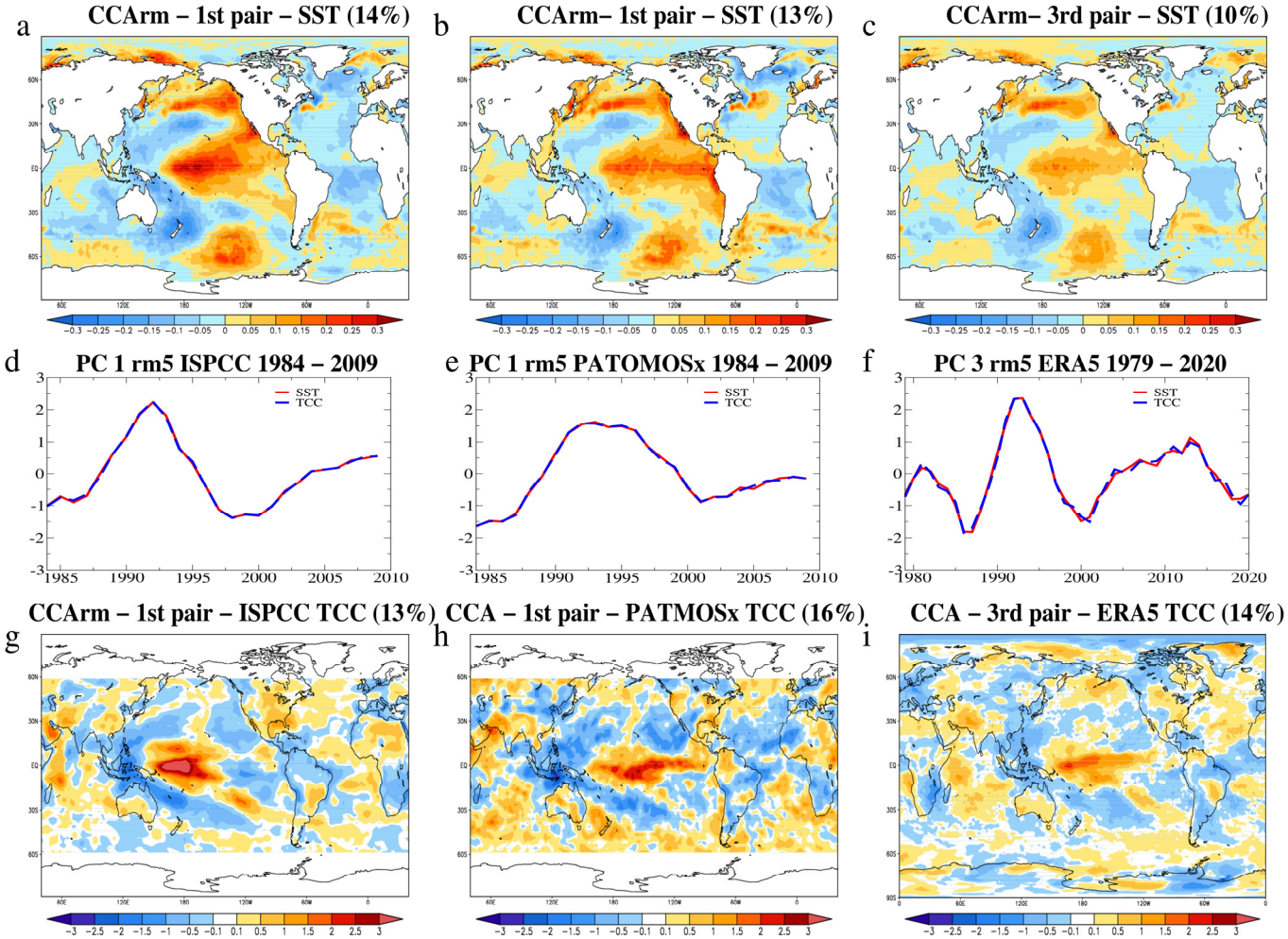

Figure 5. Pacific decadal SST variability footprint on global SST–TCC fields identified through CCA using ISPCC, PATMOS-x and ERA5 total cloud cover data filtered by a 5 yr mean. The left column shows the first coupled TCC (%)—SST (°C) pair identified through CCA using ISPCC TCC data, the SST pattern (**a**), explaining 14% of variance, the TCC structure (**g**), explaining 13% and the time series (**d**) associated with TCC (blue line) and SST (red line). The mid column shows the first coupled TCC (%)—SST (°C) pair identified through CCA using PATMOS-x TCC data, the SST pattern (**b**), explaining 13% of variance, the TCC structure (**h**), explaining 16% and the time series (**e**) associated with TCC (blue line) and SST (red line). The right column shows the third coupled TCC (%)—SST (°C) pair identified through CCA using ERA5 TCC data showing the SST pattern (**c**) explaining 10% of variance, the TCC structure (**i**) explaining 14% and the time series (**f**) associated with TCC (blue line) and SST (red line).

3.5. Associated Physical Processes

In order to investigate the physical mechanisms linking the SST–TCC anomalies and to test the robustness of the EP ENSO and the CP ENSO footprints identified through CCA, we regressed the sea level pressure (SLP), 10 m wind and total precipitation rate (TPR) fields on the time components (PCs) associated with the CP ENSO (Figure 3c), the EP ENSO (Figure 3d) and the pacific decadal variability (Figure 5d), with the results being shown in Figure 6. The regression analysis was restricted to the Tropical Pacific (30° S–30° N) for the first two ENSO modes, and to the North Pacific (0°–60° N) for the maps associated with the decadal variability. The highlighted areas correspond to a statistical significance level above 95%. Similar results were obtained for the PCs derived through rounds of CCA using the PATMOS-x and the ERA5 reanalysis TCC data.

The regression map of the SLP field of the time component associated with the EP ENSO, derived through CCA (Figure 6a), is dominated by the Southern Oscillation dipole, which is the atmospheric component of a typical El-Niño event [16,17]. The associated TPR structure (Figure 6b) presents positive anomalies from the eastern to the Central Tropical Pacific and negative loadings near Indonesia, regions in which the most severe TCC anomalies from the CCA pair linked to this mode are located (Figure 3e). The 10 m wind (Figure 6c) is convergent in the warm SST region, which, together with the SLP and TPR structure, is consistent with changes in the Walker circulation associated with the EP ENSO [69,70].

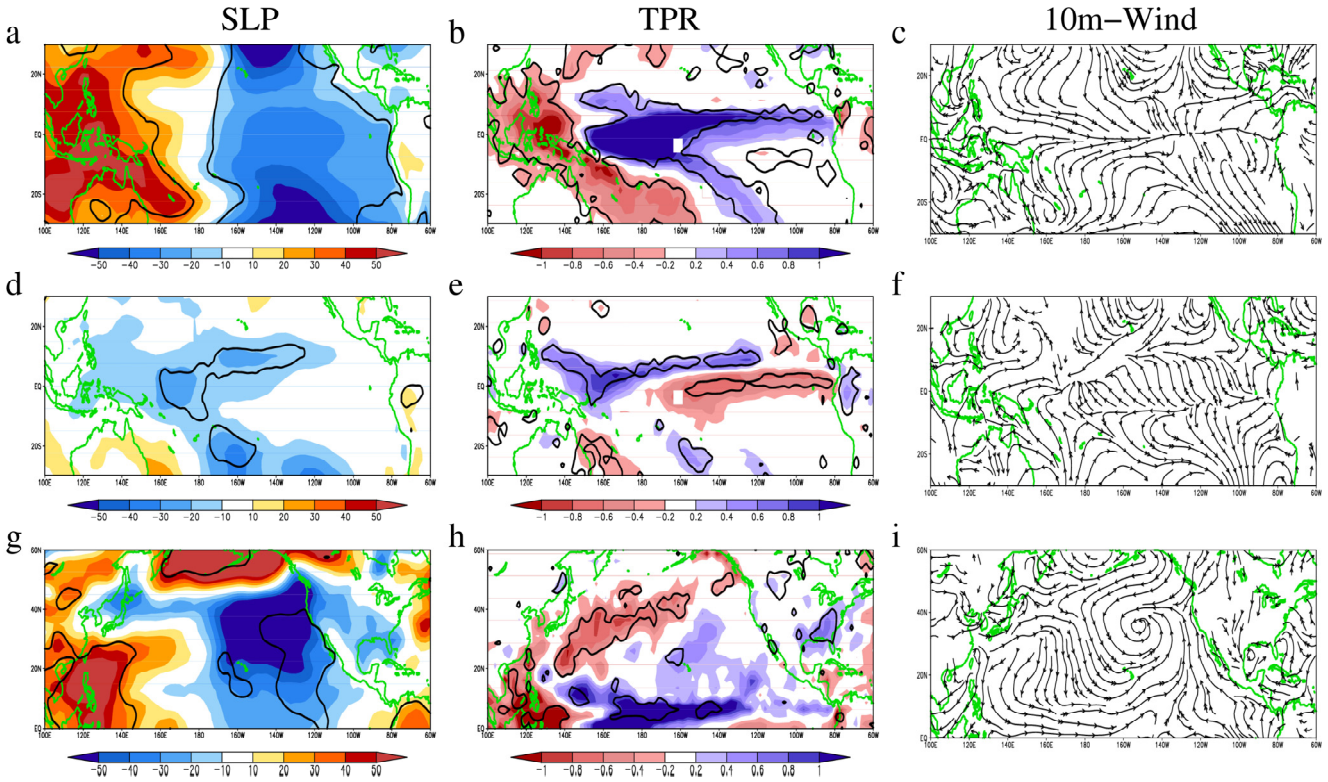

Figure 6. The regression maps of SLP (%/hPa) (left, **a**,**d**,**g**), TPR (%/mm/day) (middle, **b**,**e**,**h**) and 10 m wind (stream line) (right, **c**,**f**,**i**) fields of the time series of CCA pairs associated with EP ENSO (top row), CP ENSO (middle row) and decadal variability (bottom row) over the 1984–2009 period. The associated statistical significance in the highlighted areas is above 95%.

The SLP regression map (Figure 6d) associated with the CP ENSO is dominated by a negative V-like structure starting from the central-western Pacific and extending into the subtropics, where the positive SST anomalies from the CCA pair associated with the CP ENSO are located (Figure 3b). The TPR regression map (Figure 6e) has a dipole in the

Central Pacific with the most intense positive values in the central-western Pacific, where positive TCC anomalies from the pair associated with the CP ENSO are located (Figure 3f). These changes in TPR are related to variations in the intertropical convergence zone (ITCZ) position generated by CP ENSO [27]. The 10 m wind, TPR and SLP structures associated with the CP ENSO (Figure 6d–f) can be characterized by features that are different to those associated with the EP ENSO (Figure 6a–c) and are in good agreement with the findings of previous studies investigating the impact of the CP ENSO on these fields [23,24,27]. Of specific importance is the distinct relation between the SST and TCC anomalies in the tropics and in subtropics. In the deep tropics and in some areas in the subtropics, there is a positive correlation between the SST (Figures 2a, 3a and 4a) and TCC (Figures 2e, 3e and 4e) anomalies. This reflects a positive feedback in which relatively warm surface waters increase convection and cloud formation, mainly at high atmospheric levels [71,72]. In turn, high clouds increase the temperature at lower heights through longwave absorption and further contribute to the warming of the SSTs, which could lead to an amplification of both ENSO modes [33]. In the NE and the SE Pacific, where TCC is dominated by low level marine stratiform clouds, when the SLP is low (Figure 6a), positive SSTs (Figures 2a, 3a and 4a) are accompanied by negative TCC anomalies (Figures 2e, 3e and 4e). This reflects a distinct feedback, in which reduced cloud cover, associated with weak stability, increases the shortwave radiation fluxes toward the ocean surface and result in positive SST anomalies which, in turn, reduce low level cloudiness [31]. This feedback has been confirmed in more recent studies using numerical simulations [13] and could extend over the entire planetary ocean, not only in the regions dominated by stratocumulus clouds [14]. From this perspective, the persistence of decadal SST anomalies in the NE and SE Pacific is more related to a change in the amount of solar radiation received by the ocean due to a change in cloud cover than to ocean dynamics [45].

The TPR regression map (Figure 6h) of the PC from the CCA pair associated with decadal variability (Figure 6d) has positive values in the tropical band, where the positive areas of SST (Figure 5a) and TCC (Figure 5g) are located. Negative anomalies are seen in the western extra-tropical Pacific, coincident with negative loadings of SST and TCC. In the western extra-tropical Pacific, where a decrease in ocean temperature and cloudiness was identified (Figure 5g), negative TPR anomalies were recorded. The SLP regression map associated with decadal variability (Figure 6g) is dominated by negative anomalies in the subtropical North Pacific and positive anomalies over Alaska and around Indonesia. These features, together with the precipitation and 10 m wind spatial structures, have been previously associated with decadal variations in the Pacific basin [65,68].

4. Discussion and Conclusions

The uncertainties in the observed cloud cover data make their use for studying relatively long term natural or anthropogenic variability debatable [4,32,73–75]. In this study, interannual and decadal changes in global total cloud cover are analyzed using reliable gridded global satellite data, together with state-of-the-art reanalysis data. This provides a comprehensive picture of global TCC variability in relation to tropical Pacific climate modes. The most important modes of observed and reanalyzed global TCC variability were identified in a preliminary stage through EOF analyses and then linked through CCA to the Eastern Pacific and the Central Pacific variations of ENSO, based on their spatial and temporal properties. Both the EP ENSO- and the CP ENSO-induced TCC impacts project strongly on Pacific decadal TCC variability, with the EP ENSO being more prominent. The coupled SST–TCC footprints are physically consistent and are supported by the corresponding SLP, 10 m wind and TPR regression maps.

The identification of the EP ENSO and the CP ENSO TCC footprints in the same CCA analysis provides a better perspective on the concurrent percentages of global SST and TCC variance explained by these two modes and also allows an estimation of the impact these two modes have on decadal variability; together, the ENSO modes explain ~ 25% of the global coupled SST–TCC variance, with the CP ENSO covering half of the variance

induced by the conventional El-Niño. However, if no measures to reduce carbon emissions are implemented, we expect this percentage to increase as CP ENSO events become more frequent [23,24].

The ISPCC and PATMOS-x and ERA5 data were compared in terms of their observed impacts on EP ENSO and CP ENSO TCC. All the TCC structures identified using ERA5R fields were similar over most of the regions, with the corresponding TCC structures in ISCCP and PATMOS-x being associated with the EP ENSO and the CP ENSO, indicating that this reanalysis product reproduces observed interannual and decadal changes in global total cloud cover. Over the Pacific sector, the ISCCP, the PATMOS-x and the ERA5-reanalyzed TCC patterns look almost identical, indicating that a robust structure is associated with the EP ENSO and the CP ENSO modes, regardless of the data set or period. Across the continents, the PATMOS-x data captures the impact of the EP ENSO and the CP ENSO over the North America, South America and Australia better, making them more suitable for future regional analyses. Contrastingly, the ISCCP data seem to be more reliable for identifying decadal Pacific variations. We have shown that independent continuous CP ENSO and EP ENSO indices can be obtained based entirely on total cloud cover anomalies.

The role played by the SST—cloud interaction with respect to climate sensitivity is of critical importance in the endeavors to improve the accuracy of future climate projections [12–15,33]. Several previous studies have investigated cloud cover anomalies related to canonical ENSO [19,29–32], while the CP ENSO has been investigated in relation to high cloud cover variability [36] and local changes in precipitation [37,38]. We focused on coupled SST–TCC changes over two distinct regions: the tropical Pacific and the NE and SE subtropical Pacific. By analyzing total cloud cover fields, we have shown that, over the tropical Pacific, where cloudiness is dominated by high clouds, the positive correlation between the SST (Figures 2a, 3a and 4a) and TCC (Figures 2e, 3e and 4e) anomalies together with the negative SLP (Figure 6a) indicate that the TCC anomalies are induced by changes in SST through convection, a relation amplified by positive feedback [33,76]. However, in the NE and the SE Pacific, where total cloud cover is dominated by low level marine stratiform clouds, the negative SST (Figures 2a, 3a and 4a)/TCC (Figures 2e, 3e and 4e) correlation suggests a different feedback, through which changes in cloudiness modulate the SST, exists over this region [15,31]. However, the link between clouds and atmospheric circulation is very complex [2,12,33,46,77,78] and a consensus on the physical mechanism describing the CP ENSO has not been yet reached [18,23,24,50]. Nonetheless, the decomposition of the global total cloud cover fields, conducted in this research based on a linear combination of coupled SST–TCC pairs, could provide a reference with which one could validate the performance of general circulation models in simulating the EP ENSO and the CP ENSO dynamics.

Supplementary Materials: The following supporting information can be downloaded at: https://www.mdpi.com/article/10.3390/atmos14030456/s1; Figure S1: Regression maps of ISPCC (a,c) ((std. dev/%) and PATMOS-x (b,d) (std. dev/%) fields on the time series of the Tropical Pacific EOF structure associated with the EP ENSO (a,b) and the CP ENSO (c,d).; Figure S2: The EP ENSO (left) and the CP ENSO (right) footprints on total cloud cover identified without removing the trend from HadISST data; Table S1: The variances explained by each EOF pattern from ISPCC, PATMOS-x and ERA5R TCC data; Table S2: The variances explained by each TCC pattern obtained through CCA using ISPCC, PATMOS-x and ERA5R TCC data. References [79,80] are cited in the supplementary materials.

Author Contributions: Conceptualization, P.V.; data curation, P.V., M.V. and N.R.; formal analysis, P.V.; funding acquisition, P.V. and M.I.; investigation, P.V.; methodology, P.V., M.I. and M.V.; project administration, P.V.; resources, M.V.; software, P.V., M.I. and N.R.; supervision, M.I. and M.V.; validation, M.I.; visualization, P.V. and N.R.; writing—original draft, P.V.; writing—review and editing, M.I., M.V. and N.R. All authors have read and agreed to the published version of the manuscript.

Funding: We acknowledge support by the Open Access Publication Funds of Alfred-Wegener-Institut Helmholtz Zentrum für Polar- und Meeresforschung (AWI). This work was funded by the

Helmholtz Association through the joint program "Changing Earth-Sustaining our Future" (PoF IV) program (AWI). P.V. was financed by the project PN-III-P1-1.1-PD-2021-0505, Ctr.PD22/2022, CLIMATICFOOTPRINTS, of the Romanian UEFISCDI. M.I. and N.R. were financed by the Helmholtz Climate Initiative—REKLIM.

Institutional Review Board Statement: Not applicable.

Informed Consent Statement: Not applicable.

Data Availability Statement: All data sources are publicly available and are mentioned in the Methods section. Codes used to perform EOF and CCA analysis are available from the corresponding author.

Acknowledgments: ISCCP and PATMOS-x projects are acknowledged for the cloud data. Corrected ISCCP and PATMOS-x data were provided by the NCAR Research Data Archive. The HadISST data set was provided by the British Met Office, Hadley Centre. The Niño3 Index, the TNI and the CO2 concentration recorded at Mauna Loa Observatory were provided by NOAA/OAR/ESRL PSD, Boulder, Colorado, USA.

Conflicts of Interest: The authors declare no conflict of interest.

References

1. Zhou, C.; Zelinka, M.D.; Klein, S.A. Impact of Decadal Cloud Variations on the Earth's Energy Budget. *Nat. Geosci.* **2016**, *9*, 871–874. [CrossRef]
2. Cess, R.D.; Potter, G.L.; Blanchet, J.P.; Boer, G.J.; Genio, A.D.D.; Déqué, M.; Dymnikov, V.; Galin, V.; Gates, W.L.; Ghan, S.J.; et al. Intercomparison and Interpretation of Climate Feedback Processes in 19 Atmospheric General Circulation Models. *J. Geophys. Res.* **1990**, *95*, 16601–16615. [CrossRef]
3. Dufresne, J.L.; Bony, S. An Assessment of the Primary Sources of Spread of Global Warming Estimates from Coupled Atmosphere-Ocean Models. *J. Clim.* **2008**, *21*, 5135–5144. [CrossRef]
4. Marvel, K.; Zelinka, M.; Klein, S.A.; Bonfils, C.; Caldwell, P.; Doutriaux, C.; Santer, B.D.; Taylor, K.E. External Influences on Modeled and Observed Cloud Trends. *J. Clim.* **2015**, *28*, 4820–4840. [CrossRef]
5. Zelinka, M.D.; Grise, K.M.; Klein, S.A.; Zhoua, C.; DeAngelisb, A.M.; Christensen, M.W. Drivers of the Low-Cloud Response to Poleward Jet Shifts in the North Pacific in Observations and Models. *J. Clim.* **2018**, *31*, 7925–7947. [CrossRef]
6. Norris, J.R. Multidecadal Changes in Near-Global Cloud Cover and Estimated Cloud Cover Radiative Forcing. *J. Geophys. Res. D Atmos.* **2005**, *110*, D08206. [CrossRef]
7. Evan, A.T.; Heidinger, A.K.; Vimont, D.J. Arguments against a Physical Long-Term Trend in Global ISCCP Cloud Amounts. *Geophys. Res. Lett.* **2007**, *34*, L04701. [CrossRef]
8. Norris, J.R.; Slingo, A. Trends in Observed Cloudiness and Earth's Radiation Budget: What Do We Not Know and What Do We Need to Know? In *Clouds in the Perturbed Climate System*; Heintzenberg, J., Charlson, R.J., Eds.; Strüngmann Forum Reports; MIT Press: Cambridge, MA, USA, 2009; pp. 17–36.
9. Pallé, E. Possible Satellite Perspective Effects on the Reported Correlations between Solar Activity and Clouds. *Geophys. Res. Lett.* **2005**, *32*, L03802. [CrossRef]
10. Jacobowitz, H.; Stowe, L.L.; Ohring, G.; Heidinger, A.; Knapp, K.; Nalli, N.R. The Advanced Very High Resolution Radiometer Pathfinder Atmosphere (PATMOS) Climate Dataset: A Resource for Climate Research. *Bull. Am. Meteorol. Soc.* **2003**, *84*, 785–794. [CrossRef]
11. Norris, J.R.; Evan, A.T. Empirical Removal of Artifacts from the ISCCP and PATMOS-x Satellite Cloud Records. *J. Atmos. Ocean. Technol.* **2015**, *32*, 691–702. [CrossRef]
12. Bony, S.; Stevens, B.; Frierson, D.M.W.; Jakob, C.; Kageyama, M.; Pincus, R.; Shepherd, T.G.; Sherwood, S.C.; Siebesma, A.P.; Sobel, A.H.; et al. Clouds, Circulation and Climate Sensitivity. *Nat. Geosci.* **2015**, *8*, 261–268. [CrossRef]
13. Andrews, T.; Webb, M.J. The Dependence of Global Cloud and Lapse Rate Feedbacks on the Spatial Structure of Tropical Pacific Warming. *J. Clim.* **2018**, *31*, 641–654. [CrossRef]
14. Silvers, L.G.; Paynter, D.; Zhao, M. The Diversity of Cloud Responses to Twentieth Century Sea Surface Temperatures. *Geophys. Res. Lett.* **2018**, *45*, 391–400. [CrossRef]
15. Myers, T.A.; Norris, J.R. Reducing the Uncertainty in Subtropical Cloud Feedback. *Geophys. Res. Lett.* **2016**, *43*, 2144–2148. [CrossRef]
16. Philander, S.G. El Nino, La Nina, and the Southern Oscillation. *Int. Geophys. Ser.* **1989**, *46*, 281–289.
17. McPhaden, M.J.; Zebiak, S.E.; Glantz, M.H. ENSO as an Integrating Concept in Earth Science. *Science* **2006**, *314*, 1740–1745. [CrossRef]
18. Timmermann, A.; An, S.-I.; Kug, J.-S.; Jin, F.-F.; Cai, W.; Capotondi, A.; Cobb, K.M.; Lengaigne, M.; McPhaden, M.J.; Stuecker, M.F.; et al. El Niño–Southern Oscillation Complexity. *Nature* **2018**, *559*, 535–545. [CrossRef]

19. Chiodi, A.M.; Harrison, D.E. Global Seasonal Precipitation Anomalies Robustly Associated with El Niño and La Niña Events—An OLR Perspective. *J. Clim.* **2015**, *28*, 6133–6159. [CrossRef]
20. Cai, W.; Ng, B.; Wang, G.; Santoso, A.; Wu, L.; Yang, K. Increased ENSO Sea Surface Temperature Variability under Four IPCC Emission Scenarios. *Nat. Clim. Change* **2022**, *12*, 228–231. [CrossRef]
21. Singh, J.; Ashfaq, M.; Skinner, C.B.; Anderson, W.B.; Mishra, V.; Singh, D. Enhanced Risk of Concurrent Regional Droughts with Increased ENSO Variability and Warming. *Nat. Clim. Change* **2022**, *12*, 163–170. [CrossRef]
22. Rasmusson, E.M.; Carpenter, T.H. Variations in Tropical Sea Surface Temperature and Surface Wind Fields Associated with the Southern Oscillation/El Nino (Pacific). *Mon. Weather Rev.* **1982**, *110*, 354–384. [CrossRef]
23. Yeh, S.W.; Kug, J.S.; Dewitte, B.; Kwon, M.H.; Kirtman, B.P.; Jin, F.F. El Nĩo in a Changing Climate. *Nature* **2009**, *461*, 511–514. [CrossRef] [PubMed]
24. Ashok, K.; Yamagata, T. The El Niño with a Difference. *Nature* **2009**, *461*, 481–484. [CrossRef] [PubMed]
25. Kug, J.S.; Jin, F.F.; An, S. Il Two Types of El Niño Events: Cold Tongue El Niño and Warm Pool El Niño. *J. Clim.* **2009**, *22*, 1499–1515. [CrossRef]
26. Larkin, N.K.; Harrison, D.E. Global Seasonal Temperature and Precipitation Anomalies during El Niño Autumn and Winter. *Geophys. Res. Lett.* **2005**, *32*, L16705. [CrossRef]
27. Yu, J.Y.; Kao, H.Y.; Lee, T. Subtropics-Related Interannual Sea Surface Temperature Variability in the Central Equatorial Pacific. *J. Clim.* **2010**, *23*, 2869–2884. [CrossRef]
28. Freund, M.B.; Henley, B.J.; Karoly, D.J.; McGregor, H.V.; Abram, N.J.; Dommenget, D. Higher Frequency of Central Pacific El Niño Events in Recent Decades Relative to Past Centuries. *Nat. Geosci.* **2019**, *12*, 450–455. [CrossRef]
29. Klein, S.A.; Soden, B.J.; Lau, N.C. Remote Sea Surface Temperature Variations during ENSO: Evidence for a Tropical Atmospheric Bridge. *J. Clim.* **1999**, *12*, 917–932. [CrossRef]
30. Marsh, N.; Svensmark, H. Galactic Cosmic Ray and El Niño-Southern Oscillation Trends in International Satellite Cloud Climatology Project D2 Low-Cloud Properties. *J. Geophys. Res. Atmos.* **2003**, *108*, 4194–4195. [CrossRef]
31. Clement, A.C.; Burgman, R.; Norris, J.R. Observational and Model Evidence for Positive Low-Level Cloud Feedback. *Science* **2009**, *32*, 460–464. [CrossRef]
32. Laken, B.; Pallé, E.; Miyahara, H. A Decade of the Moderate Resolution Imaging Spectroradiometer: Is a Solar-Cloud Link Detectable? *J. Clim.* **2012**, *25*, 4430–4440. [CrossRef]
33. Radel, G.; Mauritsen, T.; Stevens, B.; Dommenget, D.; Matei, D.; Bellomo, K.; Clement, A. Amplification of El Nino by Cloud Longwave Coupling to Atmospheric Circulation. *Nat. Geosci.* **2016**, *9*, 106–110. [CrossRef]
34. Wang, H.; Su, W. The ENSO Effects on Tropical Clouds and Top-of-Atmosphere Cloud Radiative Effects in CMIP5 Models. *J. Geophys. Res.* **2015**, *120*, 4443–4465. [CrossRef]
35. Chen, Y.J.; Hwang, Y.T.; Zelinka, M.D.; Zhou, C. Distinct Patterns of Cloud Changes Associated with Decadal Variability and Their Contribution to Observed Cloud Cover Trends. *J. Clim.* **2019**, *32*, 7281–7301. [CrossRef]
36. Li, K.F.; Su, H.; Mak, S.N.; Chang, T.M.; Jiang, J.H.; Norris, J.R.; Yung, Y.L. An Analysis of High Cloud Variability: Imprints from the El Niño–Southern Oscillation. *Clim. Dyn.* **2017**, *48*, 447–457. [CrossRef]
37. Preethi, B.; Sabin, T.P.; Adedoyin, J.A.; Ashok, K. Impacts of the ENSO Modoki and Other Tropical Indo-Pacific Climate-Drivers on African Rainfall. *Sci. Rep.* **2015**, *5*, 16653. [CrossRef] [PubMed]
38. Wiedermann, M.; Siegmund, J.F.; Donges, J.F.; Donner, R.V. Differential Imprints of Distinct ENSO Flavors in Global Patterns of Very Low and High Seasonal Precipitation. *Front. Clim.* **2021**, *3*, 618548. [CrossRef]
39. Rossow, W.B.; Schiffer, R.A. ISCCP Cloud Data Products. *Bull.—Am. Meteorol. Soc.* **1991**, *72*, 2–20. [CrossRef]
40. Rossow, W.B.; Schiffer, R.A. Advances in Understanding Clouds from ISCCP. *Bull. Am. Meteorol. Soc.* **1999**, *80*, 2261–2288. [CrossRef]
41. Heidinger, A.K.; Foster, M.J.; Walther, A.; Zhao, X. The Pathfinder Atmospheres-Extended Avhrr Climate Dataset. *Bull. Am. Meteorol. Soc.* **2014**, *95*, 909–922. [CrossRef]
42. Voiculescu, M.; Usoskin, I.; Mursula, K. Effect of ENSO and Volcanic Events on the Sun-Cloud Link. *Adv. Space Res.* **2007**, *40*, 1140–1145. [CrossRef]
43. Zelinka, M.D.; Hartmann, D.L. The Observed Sensitivity of High Clouds to Mean Surface Temperature Anomalies in the Tropics. *J. Geophys. Res. Atmos.* **2011**, *116*, D23. [CrossRef]
44. Klein, S.A.; Zhang, Y.; Zelinka, M.D.; Pincus, R.; Boyle, J.; Gleckler, P.J. Are Climate Model Simulations of Clouds Improving? An Evaluation Using the ISCCP Simulator. *J. Geophys. Res. Atmos.* **2013**, *118*, 1329–1342. [CrossRef]
45. Dima, M.; Voiculescu, M. Global Patterns of Solar Influence on High Cloud Cover. *Clim. Dyn.* **2016**, *47*, 667–678. [CrossRef]
46. Vaideanu, P.; Dima, M.; Voiculescu, M. Atlantic Multidecadal Oscillation Footprint on Global High Cloud Cover. *Theor. Appl. Climatol.* **2018**, *134*, 1245–1256. [CrossRef]
47. Hersbach, H.; Bell, B.; Berrisford, P.; Hirahara, S.; Horányi, A.; Muñoz-Sabater, J.; Nicolas, J.; Peubey, C.; Radu, R.; Schepers, D.; et al. The ERA5 Global Reanalysis. *Q. J. R. Meteorol. Soc.* **2020**, *146*, 1999–2049. [CrossRef]
48. Rayner, N.A.; Parker, D.E.; Horton, E.B.; Folland, C.K.; Alexander, L.V.; Rowell, D.P.; Kent, E.C.; Kaplan, A. Global Analyses of Sea Surface Temperature, Sea Ice, and Night Marine Air Temperature since the Late Nineteenth Century. *J. Geophys. Res. D Atmos.* **2003**, *108*, 4407. [CrossRef]

49. Adler, R.F.; Huffman, G.J.; Chang, A.; Ferraro, R.; Xie, P.P.; Janowiak, J.; Rudolf, B.; Schneider, U.; Curtis, S.; Bolvin, D.; et al. The Version-2 Global Precipitation Climatology Project (GPCP) Monthly Precipitation Analysis (1979-Present). *J. Hydrometeorol.* **2003**, *4*, 1147–1167. [CrossRef]
50. Ashok, K.; Behera, S.K.; Rao, S.A.; Weng, H.; Yamagata, T. El Niño Modoki and Its Possible Teleconnection. *J. Geophys. Res. Ocean.* **2007**, *112*, C11007. [CrossRef]
51. Jeong, H.I.; Ahn, J.B. A New Method to Classify ENSO Events into Eastern and Central Pacific Types. *Int. J. Climatol.* **2017**, *37*, 2193–2199. [CrossRef]
52. Ren, H.L.; Zuo, J.; Deng, Y. Statistical Predictability of Niño Indices for Two Types of ENSO. *Clim. Dyn.* **2019**, *52*, 5361–5382. [CrossRef]
53. Trenberth, K.E.; Stepaniak, D.P. Indices of El Niño Evolution. *J. Clim.* **2001**, *14*, 1697–1701. [CrossRef]
54. Usoskin, I.G.; Voiculescu, M.; Kovaltsov, G.A.; Mursula, K. Correlation between Clouds at Different Altitudes and Solar Activity: Fact or Artifact? *J. Atmos. Sol. Terr. Phys.* **2006**, *68*, 2164–2172. [CrossRef]
55. Laken, B.A.; Čalogović, J. Solar Irradiance, Cosmic Rays and Cloudiness over Daily Timescales. *Geophys. Res. Lett.* **2011**, *38*, L24811. [CrossRef]
56. Lorenz, E.N. Empirical Orthogonal Functions and Statistical Weather Prediction. In *Technical Report Statistical Forecast Project Report 1 Department of Meteorology MIT 49*; Massachusetts Institute of Technology, Department of Meteorology: Cambridge, UK, 1956; Volume 1, p. 52.
57. North, G.R.; Bell, T.L.; Cahalan, R.F.; Moeng, F.J. Sampling Errors in the Estimation of Empirical Orthogonal Functions. *Mon. Weather Rev.* **1982**, *110*, 699–706. [CrossRef]
58. Zorita, E.; Kharin, V.; von Storch, H. The Atmospheric Circulation and Sea Surface Temperature in the North Atlantic Area in Winter: Their Interaction and Relevance for Iberian Precipitation. *J. Clim.* **1992**, *5*, 1097–1108. [CrossRef]
59. von Storch, H.; Zwiers, F.W. *Statistical Analysis in Climate Research*; Cambridge University Press: Cambridge, UK, 2002.
60. Yu, J.Y.; Kim, S.T. Identifying the Types of Major El Niño Events since 1870. *Int. J. Climatol.* **2013**, *33*, 2105–2112. [CrossRef]
61. Kao, H.Y.; Yu, J.Y. Contrasting Eastern-Pacific and Central-Pacific Types of ENSO. *J. Clim.* **2009**, *22*, 615–632. [CrossRef]
62. Trenberth, K.E.; Caron, J.M. Estimates of Meridional Atmosphere and Ocean Heat Transports. *J. Clim.* **2001**, *14*, 3433–3443. [CrossRef]
63. Garreaud, R.D.; Vuille, M.; Compagnucci, R.; Marengo, J. Present-Day South American Climate. *Palaeogeogr. Palaeoclimatol. Palaeoecol.* **2009**, *281*, 180–195. [CrossRef]
64. King, A.D.; Donat, M.G.; Alexander, L.V.; Karoly, D.J. The ENSO-Australian Rainfall Teleconnection in Reanalysis and CMIP5. *Clim. Dyn.* **2015**, *44*, 2623–2635. [CrossRef]
65. Mantua, N.J.; Hare, S.R.; Zhang, Y.; Wallace, J.M.; Francis, R.C. A Pacific Interdecadal Climate Oscillation with Impacts on Salmon Production. *Bull. Am. Meteorol. Soc.* **1997**, *78*, 1069–1080. [CrossRef]
66. Deser, C.; Alexander, M.A.; Xie, S.-P.; Phillips, A.S. Sea Surface Temperature Variability: Patterns and Mechanisms. *Ann. Rev. Mar. Sci.* **2010**, *2*, 115–143. [CrossRef] [PubMed]
67. di Lorenzo, E.; Schneider, N.; Cobb, K.M.; Franks, P.J.S.; Chhak, K.; Miller, A.J.; McWilliams, J.C.; Bograd, S.J.; Arango, H.; Curchitser, E.; et al. North Pacific Gyre Oscillation Links Ocean Climate and Ecosystem Change. *Geophys. Res. Lett.* **2008**, *35*, L08607. [CrossRef]
68. di Lorenzo, E.; Cobb, K.M.; Furtado, J.C.; Schneider, N.; Anderson, B.T.; Bracco, A.; Alexander, M.A.; Vimont, D.J. Central Pacific El Niño and Decadal Climate Change in the North Pacific Ocean. *Nat. Geosci.* **2010**, *3*, 762–765. [CrossRef]
69. Bjerknes, J. Atmospheric teleconnections from the equatorial pacific 1. *Mon. Weather Rev.* **1969**, *97*, 163–172. [CrossRef]
70. Lei, R.; Tian-Kunze, X.; Leppäranta, M.; Wang, J.; Kaleschke, L.; Zhang, Z. Changes in Summer Sea Ice, Albedo, and Portioning of Surface Solar Radiation in the Pacific Sector of Arctic Ocean during 1982–2009. *J. Geophys. Res. Ocean.* **2016**, *121*, 5470–5486. [CrossRef]
71. Back, L.E.; Bretherton, C.S. A Simple Model of Climatological Rainfall and Vertical Motion Patterns over the Tropical Oceans. *J. Clim.* **2009**, *22*, 6477–6497. [CrossRef]
72. Arking, A.; Ziskin, D. Relationship between Clouds and Sea Surface Temperatures in the Western Tropical Pacific. *J. Clim.* **1994**, *7*, 988–1000. [CrossRef]
73. Norris, J.R. What Can Cloud Observations Tell Us about Climate Variability? *Space Sci. Rev.* **2000**, *94*, 375–380. [CrossRef]
74. Probst, P.; Rizzi, R.; Tosi, E.; Lucarini, V.; Maestri, T. Total Cloud Cover from Satellite Observations and Climate Models. *Atmos. Res.* **2012**, *107*, 161–170. [CrossRef]
75. Free, M.; Sun, B. Time-Varying Biases in U.S. Total Cloud Cover Data. *J. Atmos. Ocean. Technol.* **2013**, *30*, 2838–2849. [CrossRef]
76. Hartmann, D.L.; Larson, K. An Important Constraint on Tropical Cloud—Climate Feedback. *Geophys. Res. Lett.* **2002**, *29*, 12-1–12-4. [CrossRef]
77. Sfică, L.; Beck, C.; Nita, A.I.; Voiculescu, M.; Birsan, M.V.; Philipp, A. Cloud Cover Changes Driven by Atmospheric Circulation in Europe during the Last Decades. *Int. J. Climatol.* **2021**, *41*, E2211–E2230. [CrossRef]
78. Norris, J.R.; Allen, R.J.; Evan, A.T.; Zelinka, M.D.; O'Dell, C.W.; Klein, S.A. Evidence for Climate Change in the Satellite Cloud Record. *Nature* **2016**, *536*, 72–75. [CrossRef] [PubMed]

79. Chiodi, A.M.; Harrison, D.E. El Niño impacts on seasonal US atmospheric circulation, temperature, and precipitation anomalies: The OLR-event perspective. *J. Clim.* **2013**, *26*, 822–837. [CrossRef]
80. Sulca, J.; Takahashi, K.; Espinoza, J.C.; Vuille, M.; Lavado-Casimiro, W. Impacts of different ENSO flavors and tropical Pacific convection variability (ITCZ, SPCZ) on austral summer rainfall in South America, with a focus on Peru. *Int. J. Climatol.* **2018**, *38*, 420–435. [CrossRef]